Microstructural control suppresses thermal activation of electron transport at room temperature in polymer transistors

Alessandro Luzio, Fritz Nübling, Jaime Martin, Daniele Fazzi, Philipp Selter, Eliot Gann, Christopher Mcneill, Martin Brinkmann, Michael Ryan Hansen, Natalie Stingelin, et al.

Microstructural control suppresses thermal activation of electron transport at room temperature in polymer transistors

Alessandro Luzio,[1] Fritz Nübling,[2] Jaime Martin,[3,4] Daniele Fazzi,[5] Philipp Selter,[6] Eliot Gann,[7,8,+], Christopher R. McNeill,[7] Martin Brinkmann,[9] Michael Ryan Hansen,[6] Natalie Stingelin,[10] Michael Sommer,[2,] Mario Caironi[1,]**

[1] Center for Nano Science and Technology@PoliMi, Istituto Italiano di Tecnologia, via Giovanni Pascoli 70/3, Milan, Italy
[2] Technische Universität Chemnitz, Polymerchemie, Straße der Nationen 62, 09111 Chemnitz, Germany
[3] POLYMAT, University of the Basque Country UPV/EHU, Avenida de Tolosa 72, 20018 Donostia-San Sebastián, Spain
[4] Ikerbasque, Basque Foundation for Science, 48013 Bilbao, Spain
[5] Institut für Physikalische Chemie, Department Chemie, Universität zu Köln, Luxemburger Str. 116, D - 50939 Köln, Germany
[6] Institut für Physikalische Chemie, Westfälische Wilhelms-Universität, Corrensstraße 28, 48149 Münster, Germany
[7] Materials Science and Engineering, Monash Univeristy, Clayton, Victoria 3800, Australia
[8] Australian Synchrotron, ANSTO, Clatyon, Victoria 3168, Australia
[9] Institut Charles Sadron, CNRS, Université de Strasbourg, 23 rue du Loess, BP 84047, 67034 Strasbourg Cedex 2, France
[10] School of Materials Sciences, Georgia Tech, 771 Ferst Drive, J. Erskine Love Building, Atlanta, GA, USA

[+] Present Address: National Institute of Standards and Technology, Gaithersburg, MD 20899.

*corresponding authors: m.s. michael.sommer@chemie.tu-chemnitz.de, m.c. mario.caironi@iit.it

Abstract

Recent demonstrations of inverted thermal activation of charge mobility in polymer field-effect transistors have excited the interest in transport regimes not limited by thermal barriers. However, rationalization of the limiting factors to access such regimes is still lacking. An improved understanding in this area is critical for development of new materials, establishing processing guidelines, and broadening of the range of applications. Here we show that precise processing of a diketopyrrolopyrrole-tetrafluorobenzene-based electron transporting copolymer results in highly reliable, single crystal-like and voltage-independent mobility with vanishing activation energy close to room temperature, clearly deviating from a temperature activated transport. Key factors enabling such transport behavior are uniaxial molecular alignment and thermal annealing at temperatures within the melting endotherm of films. The latter preserves chain alignment and increases crystal thickness. Experimental and computational evidence converge toward a picture of electrons being delocalized within crystalline domains of increased size. Residual energy barriers introduced by disordered regions can be effectively bypassed in the direction of molecular alignment by a more efficient interconnection of the molecularly ordered domains following the annealing process. Such rationalization of the microstructural and electronic origin of improved, non-thermally activated electron transport is crucial to redefine the limits of charge carrier mobility in polymer semiconductors and promote their implementation in high-performance devices of practical use.

1. Introduction

Semiconducting polymers with ideal, band-like transport are strongly desired to meet the requirements for a vast range of applications in the field of flexible, large-area electronics,[1, 2] including wearable, portable and distributed sensing, monitoring and actuating devices.[3, 4, 5] This need derives from a fundamental limit to the maximum charge mobility in temperature activated transport regimes, which is generally assumed to be < 1 cm^2/Vs for hopping.[6, 7] Such performance cannot meet the increasingly stringent requirements for emerging thin film technologies such as high resolution backplanes, full color displays and sensors networks, among others.

A vast library of high performance donor-acceptor copolymers has been developed in recent years, making solution processed conjugated polymers yet more appealing for large-area and flexible electronic applications.[4, 8, 9, 10, 11, 12, 13] Among them, materials with field-effect electron mobilities exceeding 1 cm^2/Vs are no longer isolated examples,[14, 15, 16, 17, 18, 19, 20, 21, 22, 23, 24, 25, 26, 27] demonstrating that n-type polymer field-effect transistors (FETs) are catching up their p-type counterparts.[12] Band-like transport in organic materials is now well established in the case of small molecules, both for single crystals[28, 29, 30, 31] and more recently for thin films.[32, 33] Likely because of the intrinsically higher degree of disorder in polymer semiconductors, very few cases of inverted temperature activated transport have been demonstrated for p-type polymer devices,[34, 35, 36, 37] and only a single one for n-type ones.[38] The observation of such inverted temperature activation has been so far assigned either to a specific chemical structure,[38] to processing conditions, [34] or to the degree of backbone alignment.[35, 36, 37] It is indeed of utmost importance to clarify the conditions necessary to observe the transition from thermal activation towards temperature independent and band-like transport in polymer FETs.

Here we report the systematic investigation of structure-function relationships in a solution-processable polymer comprising alternating dithienyldiketopyrrolopyrrole (ThDPPTh) and tetrafluorobenzene (F4) units, referred to as PThDPPThF4 (Figure 1a).[39] PThDPPThF4 used herein is synthesized by direct arylation polycondensation using a simple four-step protocol, and is free of homocoupling defects.[40] We demonstrate that the combination of uniaxial alignment and thermal annealing within the temperature range where partial melting of crystals gives access to efficient temperature-independent electron transport close to room temperature, at the boundary between temperature-activated and band-like regimes. The transport properties between these two regimes can be controlled by distinct thermal annealing protocols below, in close proximity to and above the melting temperature (T_m) of the material. Annealing at a temperature at which the smaller crystals melt, but the larger ones are maintained, allows for the thickening of the latter while preserving uniaxial chain alignment, giving rise to a gate bias-independent electron mobility of 3 cm^2/Vs. Using detailed thermal, morphological, opto-electronic and theoretical methods, we are able to assign the origin of the improved transport properties to the synergy of improved order within the crystalline domains, of increased interconnectivity of such domains, and of a significantly reduced contribution of the disordered regions. Our findings offer practical processing guidelines for microstructure engineering in high mobility polymer thin films beyond thermally limited charge transport.

2.1. Thermal characterization of PThDPPThF4 thin films

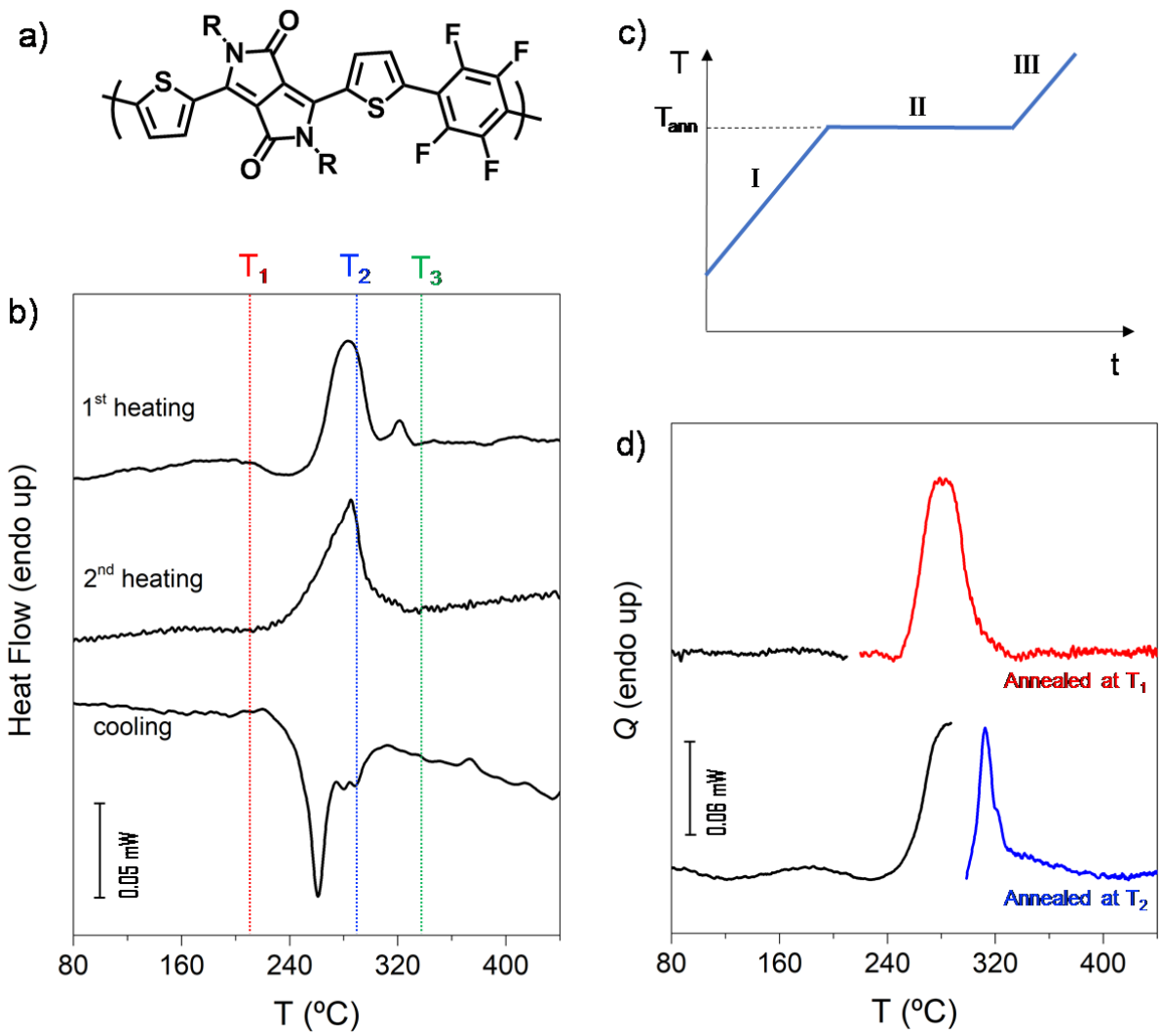

Figure 1: Fast scanning calorimetry data. (a) Molecular structure of PThDPPThF4. R= 2-octyldodecyl. (b) Fast scanning calorimetry (FSC) 1st heating, 2nd heating and cooling traces for a spin-cast thin film of PThDPPThF4 with M_n = 14 kg mol^{-1}. The three temperatures T_1, T_2 and T_3 are below, within and above the melting endotherm, respectively and used throughout this study. (c) Temperature program of isothermal annealing: stage I is the heating ramp from 30 ºC to the annealing temperature (T_{ann}) at a rate of 2000 ºC s^{-1}, stage II is a 5 min annealing period at T_{ann}, and stage III corresponds to a scan from T_{ann} to 450 ºC at 2000 ºC s^{-1}. (d) Heating traces using the isothermal annealing protocol shown in (c) with T_1 = 210 ºC and T_2 = 287 ºC. The black lines correspond to the calorimetric signal recorded as heating as spun samples up to the annealing temperatures, i.e. segment I in (c). The red and the blue lines correspond to the heating scans recorded immediately after the 5-min-annealing steps at T_1 and T_2, respectively, i.e. segment III in (c).

Thermal annealing is a widely employed strategy to enhance the transport properties of semiconducting polymer thin films via rearrangement of microstructure. Finding the optimal annealing temperature is usually either empirical or based on the phase behavior deduced from differential scanning calorimetry (DSC) performed on bulk samples. However, it is well-known that the phase behavior of bulk polymer materials often differs from that of thin films,[41] which are typically employed in FETs. Furthermore, in the spin casting process the polymer rapidly solidifies, giving rise to a kinetically trapped, non-equilibrium microstructure. Hence, the direct correlation between the phase behavior, including the thermal transitions, of spin coated thin films and standard DSC data is not always accurate. In order to assess the thermal behavior and the effect of thermal annealing on PThDPPThF4 thin films processed under the conditions employed in FET devices, we conducted fast scanning calorimetry (FSC) instead of standard DSC experiments. FSC offers several advantages compared to standard DSC when elucidating the phase behavior of semiconducting polymers.[42] Firstly, the high scanning rates of up to 50000 ºC s^{-1} allow for the analysis of very thin films, which can be spin cast from solutions directly onto chip-sensors. Secondly, the microstructure developing during processing can be investigated because (i) the excellent thermal contact between the thin film and the chip-sensor allows for a reliable evaluation of the first heating curves and (ii) the fast heating rates may avoid further structural reorganization during the heating scan.[43] Equally important is that temperature windows outside common stability ranges of the materials become accessible as thermo-oxidative degradation at high temperatures is largely avoided because of the scanning rate.[44] For a complete discussion of DSC vs. FSC see the Supplementary Information (SI).

The FSC traces of the 1st and the 2nd heating and the 1st cooling scans of a spin cast, ~ 40 nm thin PThDPPThF4 film (number-average molecular weight, M_n: 14 kg mol^{-1}; dispersity, $Đ$: 3.7) at a scan rate of 2000 ºC/s are shown in Figure 1b. We associate the main endothermic peaks in heating scans with melting of the crystalline regions of PThDPPThF4. As such, the melting temperatures (T_m) for the as-cast (1st heating scan) and the melt-crystallized (2nd heating scan) samples amount to 283 and 285 ºC, respectively. Likewise, the main exothermic peak at 261 ºC in the cooling trace corresponds to crystallization of PThDPPThF4. Because the 1st heating trace in Figure 1b reflects the microstructure developed during spin coating, it can be used as a guide to judiciously select annealing temperatures. Accordingly, the annealing temperatures T_1, T_2 and T_3 were selected as temperatures well-below, within and above the melting endotherm, respectively. At T_3, PThDPPThF4 is in the liquid state where molecular order is lost, and the final microstructure of the film at room temperature depends on the cooling kinetics. Conversely, PThDPPThF4 films are semicrystalline when annealed at T_1 and T_2 and thus the impact of annealing at those temperatures can be evaluated by calorimetry. In order to do so, we designed the thermal protocol shown in Figure 1c. T_1 = 210 ºC and a T_2 = 287 ºC were selected according to the data presented in Figure 1b. Classical isothermal crystallization experiments in which films are quenched from the melt to a pre-selected crystallization temperature were not considered so as not to erase backbone alignment. The black traces in Figure 1d correspond to the calorimetric signal recorded when heating an as-spun film up to the annealing temperature (stage I, Figure 1c). The red and the blue traces correspond to the heating scans recorded immediately after the isothermal 5

min periods at T_1 and T_2, respectively (stage III). We find that annealing at T_1 has no impact on the melting behavior, as expected. On the contrary, annealing at T_2 provokes a marked shift of the melting endotherm towards higher temperatures with T_m increasing by more than 29 ºC with respect to the T_m of the pristine films and films annealed at T_1. The increase in T_m can be rationalized in terms of thickening of the crystalline lamellae during annealing at T_2, in agreement with the Gibbs-Thomson theory.[45] Accordingly, in PThDPPThF4 films annealed at a temperature within the melting temperature range, the thinner crystalline lamellae melt, while the thicker lamellae remain solid and evolve towards the thermodynamic equilibrium structure, which corresponds to crystals where chains are fully extended.[46] Therefore, during annealing at T_2, the thickness of the solid lamellae significantly increases, which results in the observed, notable increase of T_m (for further discussion of crystal reorganization see SI). This behavior is common to all PThDPPThF4 samples analyzed, independently on chain length and molecular characteristics, as demonstrated in the SI for samples of M_n = 11, 14 and 30 kg mol^{-1} (Figure S6). Further confirmation comes from measurements performed at lower scanning rates, using standard DSC and optical microscopy and spectroscopy (see Figures S5, S7-S9).[43, 47]

2.2. Optical Characterization of Aligned Films

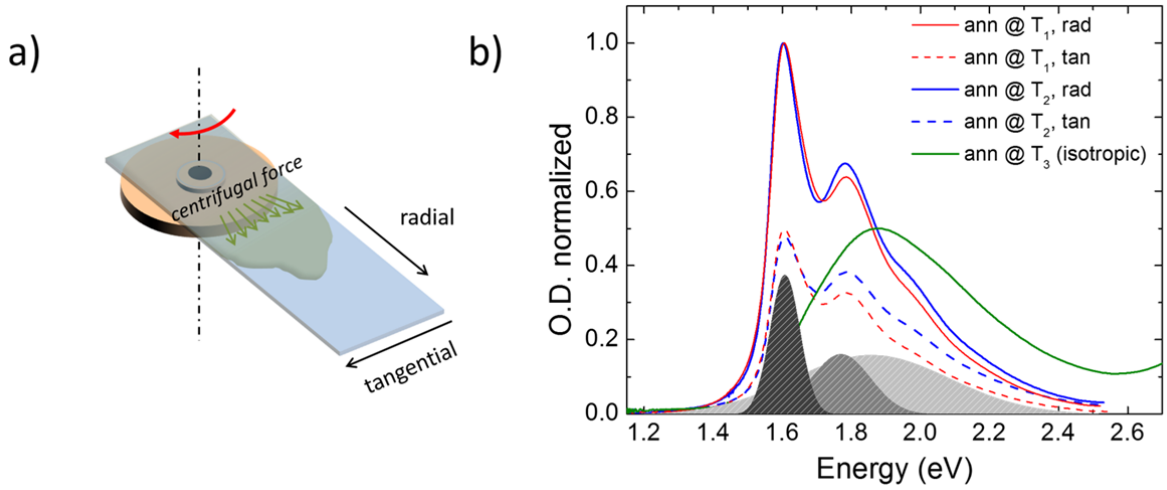

Figure 2: Uniaxial alignment and optical anisotropy. a) Schematic of the off-center spin coating deposition method; b) polarized UV-Vis spectra of films aligned using off-center spin coating and subsequently annealed at T_1, T_2 and T_3. The grey filled Gaussians are fittings of films annealed at T_1 and T_2.

A strong enhancement of charge mobility in polymer semiconductors can be obtained with uniaxial backbone alignment, inducing transport anisotropy and favoring improved transport properties along the alignment direction.[48] To exploit such behavior, we have realized uniaxially aligned films using either off-center spin coating (Figure 2a), or wired-bar coating, according to a methodology based on the exploitation of marginal solvents and directional flow during deposition.[14, 49] These two techniques produce similarly aligned and microstructured films.

Figure 2b shows UV-Vis spectra of aligned films after annealing at T_1, T_2 and T_3. All spectra feature a low energy (namely, charge transfer or CT band) and a high energy (not shown) band. While significant spectral changes between films annealed at T_1 and T_2 cannot be observed, a strong hypsochromic shift occurs after melt-annealing at T_3. Spectra of films annealed at T_1 and T_2 show three contributions, two bands at low energy (≈1.60 eV and ≈1.77 eV) assigned to 0-0 and 0-1 transitions within PThDPPThF4 aggregates, and a shoulder peaking at ≈1.88 eV, which is assigned to disordered polymer chains.[40] Following this assignment, we can observe that the content of crystalline regions is similar for films annealed at T_1 and T_2, despite the population of thicker crystallites after annealing at T_2. Upon melt annealing at T_3 and successive cooling, the thermal history of the film is erased. As a consequence, the band at 1.88 eV dominates the spectrum owing to an increased molecularly disordered structure.

Measurements of the dichroic ratio (*DR*) reveals optical anisotropy after annealing at T_1 and T_2 ($DR \approx 2$ in both cases), implying preferential alignment of polymer chains along the radial direction induced during off-center spin coating. It is important to emphasize that uniaxial alignment is maintained upon annealing at T_2, which is a consequence of the thicker crystals acting as nuclei that dictate chain and crystal orientation. In contrast, melting at T_3 followed by cooling to room temperature entirely erases any preferred backbone alignment.

2.3. Microstructural Characterization of Aligned Films

Grazing incidence wide-angle X-ray scattering (GIWAXS) was employed to gain information on how annealing processes modify morphology and coherence lengths. d-spacings and coherence lengths from two-dimensional GIWAXS pattern are summarized in Table 1 (for GIWAXS patterns see Figs. S10-S11). The sample annealed at T_1 shows a semicrystalline morphology with pronounced edge-on orientation of chains (as evaluated through Herman's S-parameter, $S = 0.49$, Fig. S12 and Table S2). The main chain-side chain separation (100 reflection) and π-stacking (010 reflection) distances are 2.04 nm and 0.37 nm, respectively. Upon annealing at T_2, both the main chain-side chain separation distance and the π-stacking distances increase to 2.11 nm and 0.38 nm, respectively. A population of face-on crystallites appears, which shifts the S-value to $S = 0.32$. The coherence lengths in both stacking directions improve considerably compared to films annealed at T_1: from 13.7 nm to 16.45 nm for the (100) and from 5.37 nm to 7.28 nm for the (010) reflection. This is a clear indication of an increased crystal dimension upon annealing at T_2, in agreement with the FSC data. Melt-annealing at T_3 results in a major loss of crystalline scattering features, in agreement with optical characterization (Figure 3). In the sample annealed at T_3, mainly diffuse scattering from weakly correlated side-chain stacking and π-stacking is observed, indicative of a prevalently amorphous film. Only the π-stacking distance of a minor residual crystalline fraction is still seen, but is significantly larger, ~ 0.44 nm, while the coherence length is strongly reduced to 1.36 nm. Thus, T_3 annealed films are weakly crystalline and characterized by much smaller and more disordered crystallites.

Table 1. Summary of d-spacings and coherence lengths for alkyl- and π-stacking as derived from analysis of the GIWAXS data (see SI, Section 2.7).

	(100) main chain side chain separation		(010) (π-stacking)	
Sample	d-spacing (nm)	Coherence Length (nm)	d-spacing (nm)	Coherence Length (nm)
T_1	2.04	13.70	0.37	5.37
T_2	2.14	16.45	0.38	7.28
T_3	-	-	0.44	1.36

Near-edge X-ray absorption fine structure (NEXAFS) spectroscopy measurements on aligned films (Figure S14)[50] support the view of a strong in-plane alignment of polymer chains at the surface of films annealed at T_1 and T_2, with mostly identical dichroic ratios (calculated as the maximum resonance intensity of the carbon 1s-π* transition divided by the minimum resonance intensity) of 6.6 upon annealing at T_1 and 6.1 for annealing at T_2. In general, *all* annealed films exhibit a more marked edge-on orientation of polymer backbones at the surface compared to the bulk (tilt angle values comprise between 62° and 66°, Table S2).

TEM analysis of films annealed at T_1 and T_2 (Figure 3a,b) shows in-plane π-stacking peaks of mostly edge-on oriented crystallites, and sharper π-stacking reflection upon T_2 annealing, indicating an increased crystalline order, in agreement with GIWAXS analysis. The samples annealed at T_1 show some reflections along the chain direction at 2.7 Å and 2.3 Å, suggesting periodic ordering of the monomeric units. In the sample annealed at T_2, no more reflections are seen along the chain direction supporting a mechanism of disordering in the overlap of successive chains within the π-stack. This situation is similar to that recently observed in a different low bandgap polymer, namely PCE11.[51] In PCE11, a segregated stacking between benzothiadiazole and quaterthiophene units is observed for low crystallization temperatures and a disordered stacking of the two units for temperatures close to the melting. From a morphology point of view, a lamellar periodic structure with a 28 nm period (Figure 3b) is apparent after annealing at T_2. This situation is reminiscent of the naphthalene diimide bithiophene co-polymer for which a transformation of form I to form II upon thermal annealing results in a similar morphological change from a fibrillar morphology in pristine films (form I) to a periodic lamellar morphology (form II).[52]

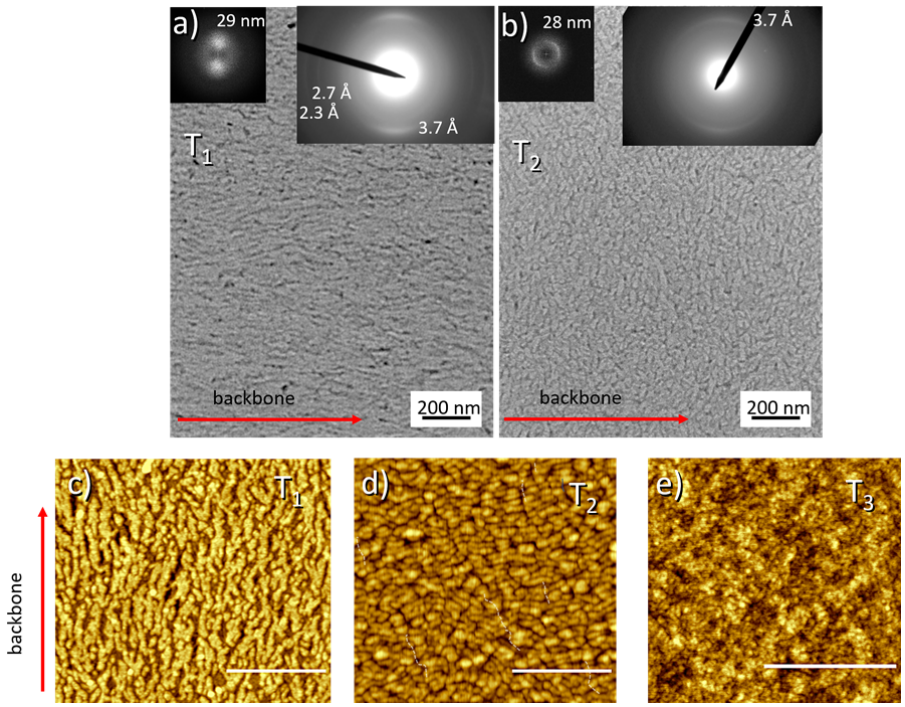

Figure 3: Microscopic characterization. a,b) TEM analysis of T_1- and T_2-annealed films with insets showing electron diffraction; c-e) AFM topography images of oriented films annealed at T_1 ($R_{r.m.s.}$= 1.2), T_2 ($R_{r.m.s.}$= 0.62), and T_3 ($R_{r.m.s.}$= 0.54) (scale bar for AFM images: 500 nm).

In Figure 3c-e atomic force microscopy (AFM) topography images are reported. Whisker-like elongated superstructures can be observed on the surface of films annealed at T_1 (Figure 3c), clearly aligned along the radial direction of spin. Upon annealing at T_2 (Figure 3d), the whiskers transform into crystalline lamellae of ~30 nm thickness, which apparently are oriented perpendicular to the radial direction of the spin (i.e. chains being aligned radially to the spin), in agreement with TEM analysis (Figure 3b). Backbone direction, however, does not change upon annealing at T_2. After solidification from T_3 (Figure 3e), the top surface is composed of small domains that lack any evidence of an ordered structure.

2.4. Local packing from solid state NMR

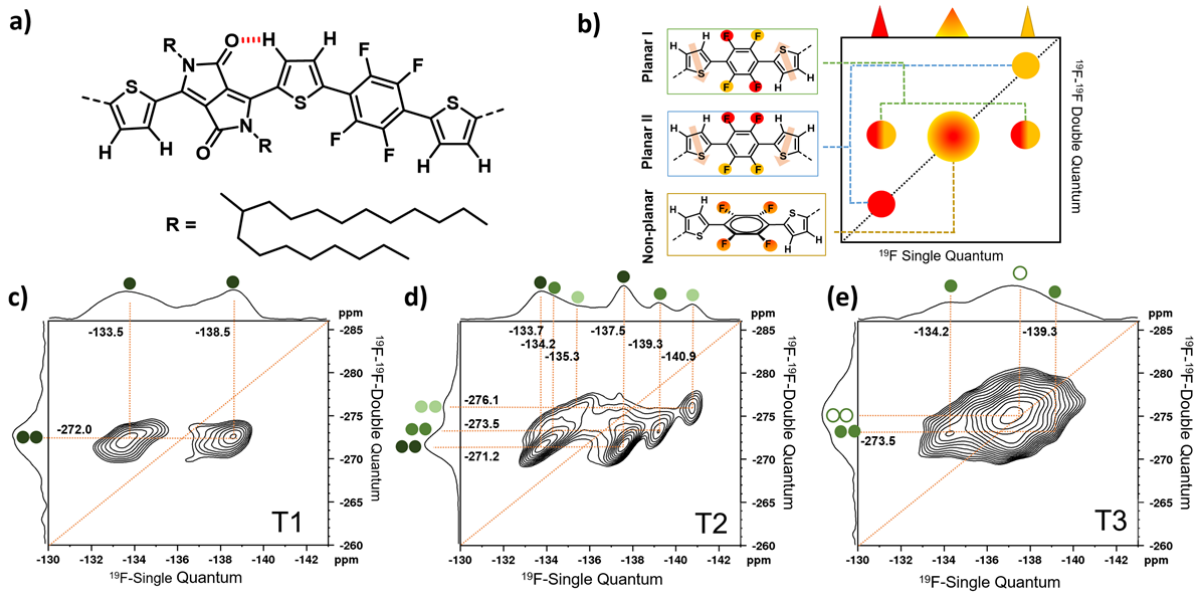

Figure 4: Solid-state NMR data. Results from ^{19}F-^{19}F solid-state NMR. (a) Conformation of the polymer backbone inside the ordered domains after annealing at T_1. (b) schematic representation for the interpretation of the ^{19}F-^{19}F DQ-SQ correlation spectra shown in (c) to (e): while only one broad pair of cross-correlations is observed after annealing at T_1, three new cross-correlation pairs with significantly narrower lines are observed after annealing at T_2. Annealing at T_3 leads to mostly non-planar conformations around the F4 monomer.

To gain detailed information about temperature-dependent polymer chain conformation and the local molecular packing of PThDPPThF4, we performed solid-state ^{1}H and ^{19}F magic-angle spinning (MAS) NMR experiments on samples annealed at different temperatures. These experiments rely on the reintroduction of the homonuclear ^{1}H-^{1}H and ^{19}F-^{19}F dipolar coupling via 2D double-quantum single-quantum (DQ-SQ) NMR correlation experiments,[53] providing molecular information about spatial proximities and chain conformations.[54, 55] In addition, 2D ^{1}H-^{13}C heteronuclear correlation (HETCOR) spectroscopy experiments were performed. Like the ^{1}H and ^{19}F MAS NMR techniques, these experiments utilize the heteronuclear direct dipolar coupling to transfer magnetization directly through space from ^{1}H to ^{13}C, thereby offering the potential to establish through-space interchain correlations.

On the basis of the observations from 2D ^{1}H-^{1}H DQ-SQ and ^{19}F-^{19}F DQ-SQ NMR correlation spectra, all reported in Section 2.9 of SI, it can be concluded that the amorphous-like phase of the samples is characterized by a non-planar Th-F4-Th conformation and less ordered aliphatic side chains. Conversely, a strongly planarized molecular conformation is observed within the ordered domains of the samples annealed at T_1 and T_2.

Annealing at T_1 leads to a single stacking configuration for PThDPPThF4 in its ordered domains, with one prevalent polymer conformation as schematically illustrated in Figure 4a. This conformation includes (i) an

263 intramolecular hydrogen bond between the DPP and neighboring Th group, as well as (ii) a co-planar 'anti'
264 conformation of the thiophene groups surrounding the F4 units. Combining ^{1}H-^{1}H DQ-SQ and ^{19}F-^{19}F DQ-
265 SQ correlation data with insights from ^{1}H-^{13}C HETCOR data (Figure S22), we propose a packing model for
266 the polymer in the ordered domain, with the DPP units of one chain being placed above/below the F4 units
267 of neighboring polymer chains. While this arrangement places an electron-deficient DPP unit above another
268 electron-deficient F4 unit, it maximizes the distance between the sterically demanding aliphatic side chains,
269 suggesting that the formation of this packing mode is at least partially driven by a reduction in steric
270 hindrance. Taken together, this leads to the packing model I shown in Figure 5b, corresponding to a shifted
271 packing of the PThDPPThF4 main chains, where the DPP units are sandwiched in between F4 units from
272 above and below.
273 Going to the higher annealing temperature T_2, no significant changes in conformation in the ordered domains
274 are observed from both ^{1}H and ^{19}F NMR spectra. However, ^{1}H-^{1}H DQ-SQ correlation data indicates an
275 increase in the order of the aliphatic side chains (Figure S18), while ^{19}F-^{19}F DQ-SQ correlation data shows
276 the occurrence of three distinct cross-correlation peaks, with different chemical shifts compared to the
277 correlations observed for T_1 (Figure 4c to 4e). Since any conformational change around the F4 unit should
278 result in either the occurrence of one or two auto-correlations (Figure 4b), the emergence of three distinct
279 cross-correlation peaks clearly indicates the formation of at least two new packing modes, henceforth
280 referred to as packing mode II and III (Figure 5c,d). The structure of these two packing modes can be
281 deduced by combining the results of ^{1}H and ^{19}F MAS NMR with further ^{1}H-^{13}C experiments, establishing a
282 picture where packing modes II and III emerge from mode I via a slip of the polymer chains along their long
283 axes, placing the DPP and F4 units now above neighboring Th units. This places the electron-deficient
284 groups above and below electron-rich Th units, likely resulting in a lower overall energy. Sliding of the
285 polymer backbones is possibly facilitated by an increase in order of the aliphatic chains, resulting in less
286 steric demand in the long-axis direction of the polymer backbone and, as evident from GIWAXS, in an
287 increased main chain-side chain separation distance with respect to T_1.
288 Since for every DPP and F4 unit two Th units are present in the polymer chain, the slip can occur in two
289 directions (Figure 5e) leading to the formation of either packing mode II or III. Interestingly, packing mode
290 II retains point reflection symmetry in the F4 unit, resulting in two of the ^{19}F sites at the F4 unit being
291 equivalent, while this symmetry is no longer present in mode III, where all four ^{19}F sites at the F4 unit are
292 inequivalent.
293 Heating above the melting temperature at T_3 breaks a large fraction of the co-planar 'anti' conformations of
294 the F4 group with respect to the neighboring Th units, increasing dihedral angles and leading to a packing
295 structure of PThDPPThF4 dominated by random intra-chain conformations.

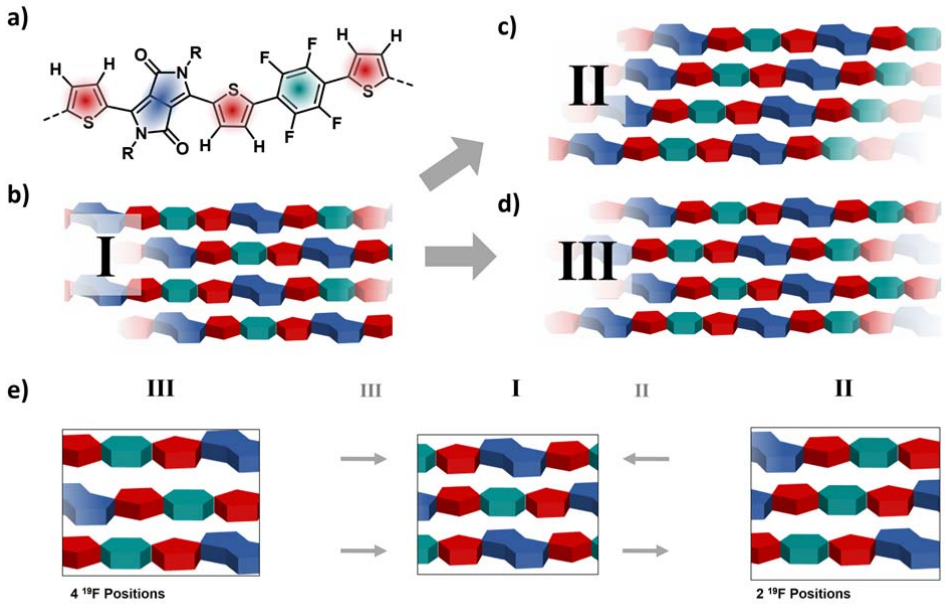

Figure 5: Molecular packing. Schematic representation of local packing from solid-state NMR. (a) The predominant conformation in the ordered domains is characterized by an intra-molecular hydrogen bond and the 'anti' configuration of the thiophene monomers next to the F4 unit; (b) packing model I for the ordered domains after annealing at T_1, which upon annealing at T_2 transforms into packing models II (c) and III (d). The three models are connected via a slipping motion involving the both neighboring chains moving in either the same or opposite directions (e).

2.5. Room temperature FETs electrical characterization

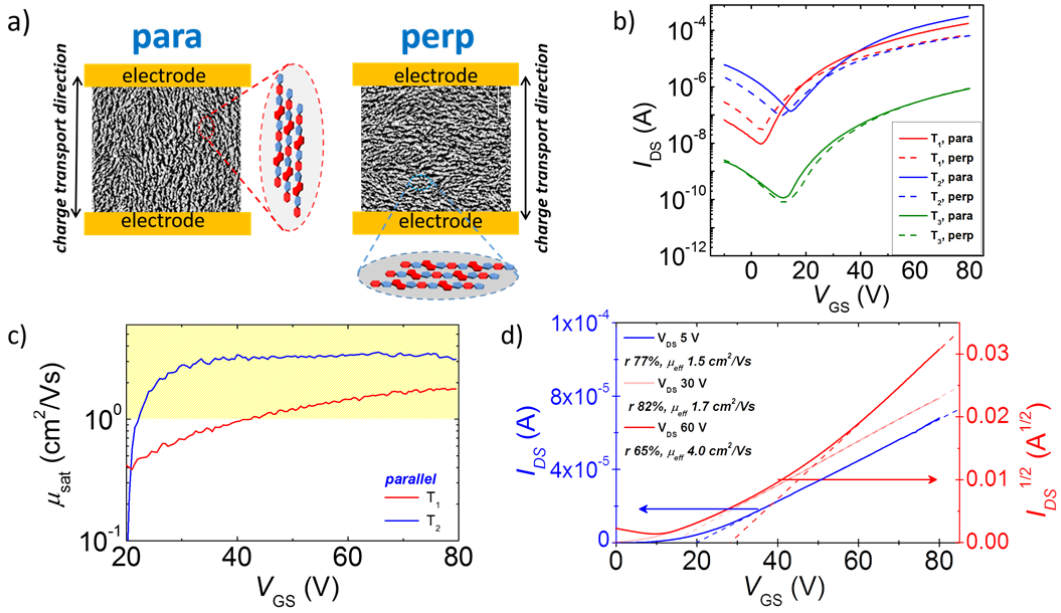

Figure 6: Electrical data of FETs. FET characterization of PThDPPThF4. (a) Sketch of source and drain pattern configuration parallel (*para)* and perdendicular (*perp)*, allowing to probe transport parallel and perpendicular to the chain direction, respectively; (b) transfer curves (W = 1000 µm L = 80 µm), deposited using off-center spin coating, annealed at T_1, T_2 and T_3 and probed parallel and perpendicular to chain direction; (c) saturation mobility values (μ_{sat}) vs. V_{GS} plot of films annealed at T_1, T_2 probed parallel to chain direction; (d) transfer curves after annealing at T_2 (W = 1000 µm L = 100 µm) including an injection interlayer at V_{DS} = 5 V, V_{DS} = 30 V and V_{DS} = 60 V; FET parameters of curves in (d): W = 1000 µm; L = 100 µm; Ci = 5.7 nF/cm^2.

We fabricated bottom-contact, top-gate FETs using uniaxially aligned PThDPPThF4 thin films and a ≈550 nm thick PMMA dielectric layer. For uniaxial alignment, we employed alternatively off-center spin coating, as for optical and structural characterization samples, and wired-bar coating, a fast, large-area and scalable directional printing process.[14]

To avoid extrinsic phenomena such as contact resistance and current-induced self-heating (Joule effect) leading to a questionable extraction of intrinsic transport parameters,[7, 56, 57, 58] FETs with a large channel length (from 80 µm to 100 µm) were mainly employed for mobility extraction. For comparison, *I-V* curves of devices with 20 µm long channels are additionally reported in SI.

The transport properties were investigated both with backbone alignment orientation parallel (Figure 6a**,** ***para*** source & drain configuration) and perpendicular (Figure 6a, ***perp*** source & drain configuration) to the charge transport direction (as defined by the orientation of electrical contacts). In Figure 6b, representative transfer curves of FETs with 80 µm channel length are shown (output curves are reported in Figure S25b and S26b). All devices exhibit typical ambipolar V-shaped curves with a clear prevalence for *n*-type current modulation and a weak p-type current appearing below 10 V. Gate leakage current is always much lower than drain-source current in all the explored voltage range (Figure S25a and S26a). Backbone alignment results in charge transport anisotropy with improved transport properties along the direction of polymer backbones (*para*, Figure 6b). In films annealed at T_1, a 2.6× higher source to drain current (I_{DS}) is recorded with respect to *perp* configuration at the maximum V_{GS} employed in saturation regime. In films annealed at T_2, the $I_{DS,para}/I_{DS,perp}$ ratio increases to ≈ 5, owing to an improvement of transport only in the parallel direction. In films processed at T_3, transport anisotropy is no longer present, in agreement with the loss of uniaxial alignment, and a general drop of current is observed.

Apparent saturation mobility values were first extracted from the local slopes of $I_{DS}^{1/2}$ vs. V_{GS} for the saturation regime and of I_{DS} vs. V_{GS} for the linear regime, according to the gradual channel approximation equations.[59] Focusing on the transport properties parallel to backbone alignment (Figure 6c), for films annealed at T_1, gate voltage-dependent mobility values are extracted within the entire investigated range, i.e. up to V_{GS} = 80 V. At the maximum applied V_{GS} the maximum apparent mobility extracted is ≈ 1.7 cm^2/Vs. Such marked voltage dependence of mobility in a long channel polymer transistor where contact effects

should be mitigated can be associated to charge density transport dependence in a broad density of states (DOS) and/or trap filling.[60, 61]

More interestingly, upon annealing at T_2, the apparent mobility value parallel to backbone alignment (μ_{para}) rapidly saturates to a constant value at relatively low V_{GS} > 30 V, i.e. just 10 V above the threshold voltage V_{Th} (Figure 6c), denoting more ideal transport characteristics. Moreover, the electron mobility is found to exceed 1 cm^2/Vs for V_{GS} values very close to V_{Th} (*i.e.* at the early onset of the device). To further reduce V_{Th}, we implemented an injection layer into the device (see details in SI, Figure S27, and transfer curves in Figure 6d), leading to a reduction of V_{Th} by ~ 5 V with no variation of mobility values. This is indicative of a contact resistance-dominated turn-on voltage which may be further engineered and improved.

As a more reliable parameter and to take into account device non-idealities, we extracted the effective mobility μ_{eff} as the product between the apparent mobility and the measurement reliability factor r, as recently defined by Choi et al.[62] In Figure 6d, I_{DS} vs. V_{GS} and $I_{DS}^{1/2}$ vs. V_{GS} curves for T_2 annealed films, both in linear and saturation regime, from devices with an injection layer are reported. Current values are recorded parallel to the alignment direction. It is worth noting that μ_{eff} of ≈ 1.5 cm^2/Vs is obtained already in the linear regime (V_{DS} = 5 V), as a result of a high reliability factor of ≈ 77 %. Such a high r value indicates FET behavior not far from ideality. In the present case the reliability factor is mostly limited by the non-zero threshold voltage. As a confirmation, at the onset of the saturation regime (V_{DS} = 30 V), an r up to ~ 82% is extracted, due to a reduced threshold voltage of V_{Th} = 14 V. Moreover, a notable μ_{eff} value of ≈ 4 cm^2/Vs is obtained at V_{DS} = 60V (r = 65%, μ_{sat} = 6.1 cm^2/Vs). It is worth highlighting that the high reliability values for films annealed at T_2 compare well to those obtained with polymeric *p-type* counterparts and, remarkably, with small molecule thin films and single crystal based devices, leading to impressively high effective mobilities.[27, 63, 64, 65] When films are subjected to a temperature above melting (T_3), the mobility drastically decreases to 10^{-2} cm^2/Vs and a strong V_{GS} dependence of the mobility is observed. Such electrical behavior is in agreement with increased microstructural/conformational disorder and consequently strong DOS broadening as suggested by the above optical and microstructural characterization.

2.6. Variable temperature FETs electrical characterization

It has been predicted that for charge mobility values exceeding 1 cm^2/Vs, the transport regime must clearly deviate from a thermally activated mechanism, typically observed in most polymer semiconductors.[6] In order to get insight into the transport mechanism that is operative in aligned films of PThDPPThF4, we performed electrical characterization at variable temperature (Figure 7). In the notable case of films annealed at T_2, the μ_{perp} vs. $1/T$ plot can be well described by an Arrhenius dependence over the entire temperature range, with an activation energy E_a of ≈100 meV at any V_{GS} employed for mobility extraction (Figure S30). Differently, at sufficiently high V_{GS}, μ_{para} is constant down to 280 K. This observation is reproducible in different devices and with different dielectrics (see Figure S31) and reveals a temperature range in which transport is not thermally activated, suggesting a transition to a band-like regime. For temperatures below 280 K, thermally activated transport is instead observed with E_a = 61 meV. Within the thermally activated low temperature

range, a reduced E_a is found (from 61 meV to 31 meV) when a low-κ dielectric layer like Cytop (κ = 2.1) is employed instead of PMMA (κ = 3.6), indicating a dielectric-induced dipolar disorder effect on the DOS, dominating low temperature operation.[66, 67, 68, 69, 70, 71, 72] Overall, according to a mobility edge model, a scenario is suggested where shallow traps dominate below a threshold temperature of 280 K, above which thermal fluctuations enable charge releasing to extended mobile states.[61] Data on films annealed at T_1 and T_3 are also displayed in Figure 7. For both temperatures, purely thermally activated transport is found over the entire temperature range investigated, with extracted activation energies of ≈140 meV and ≈100 meV for T_3 and T_1, respectively.

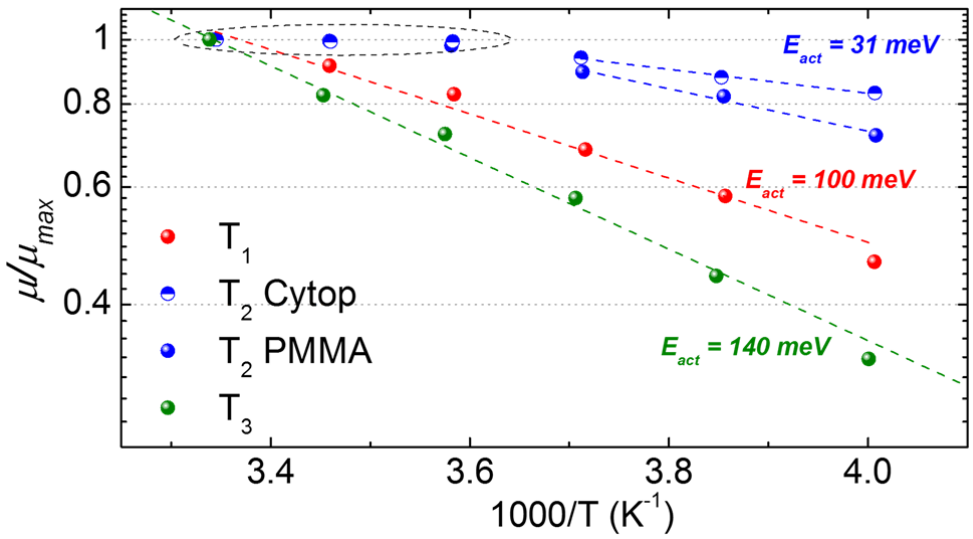

Figure 7: Mobility as a function of temperature. Comparison of μ_{para}/μ_{max} vs. $1/T$ from the OFETs of this work in the direction parallel to backbone alignment.

2.7. Charge Modulation Spectroscopy and Microscopy

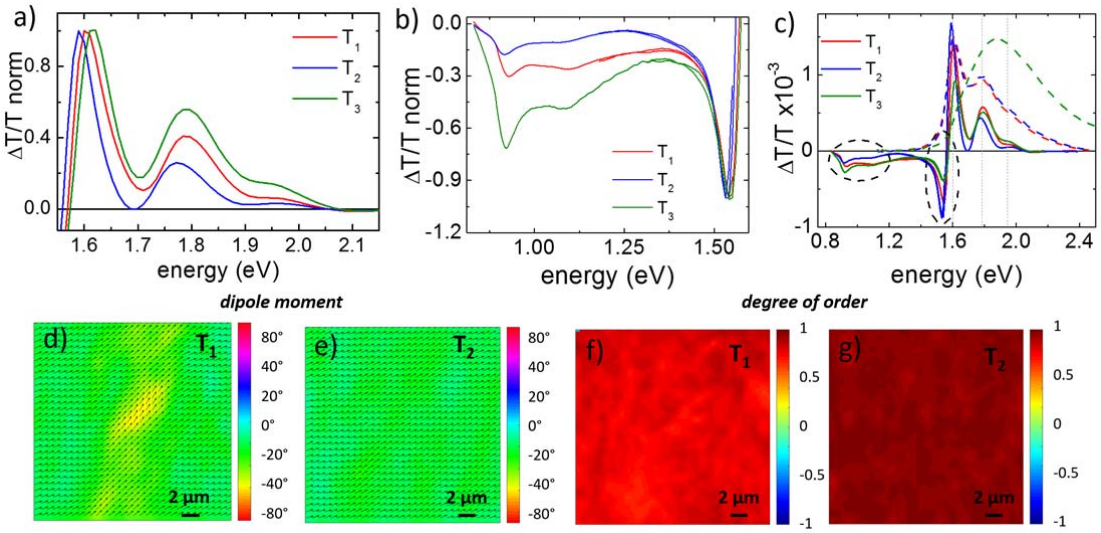

Figure 8: Charge modulation micro-spectroscopy. Normalized CMS spectra of PThDPPThF4 in the high energy range (from 1.7 to 2.15 eV) (b) and low energy range (from 0.5 to 1.55 eV) (c); (c) CMS spectra of PThDPPThF4 annealed at T_1, T_2 and T_3, driven at V_{GS} = 20 V; normalized optical density spectra (dashed lines) are also reported; 20 × 20 µm^2 polarized CMM maps with the indication of the polymers backbone orientation (d,e) and the relative degree of orientational order (f,g) of PThDPPThF4 films annealed at T_1 (d,f) and T_2 (e,g).

Charge modulation spectroscopy (CMS) was employed to investigate charge induced optical signatures (i.e. polaronic relaxations) in FETs of PThDPPThF4. The $\Delta T/T$ spectra obtained in FETs with active layers annealed at the different temperatures show all a positive bleaching signal between 1.55 eV and 2.0 eV. This signal is composed of two positive peaks at 1.6 eV and 1.75 eV, and a shoulder peaking at around 1.9 eV. Furthermore, two main negative contributions at lower energies in the near infra-red (NIR) region are found: a narrow one, peaking around 1.55 eV, overlapping with bleaching, and a much broader band having defined peaks at 0.9 and 1 eV (Figure 8a,b). Downstream interpretation of the CMS spectra allows to confidently associate $\Delta T/T < 0$ signals to polaronic optical transitions and $\Delta T/T > 0$ to the bleaching of ground-state absorption. Negligible electro-absorption effects are present, as detailed in the SI, where an accurate investigation aimed at evaluating the presence of a Stark effect due to electric field modulation within the semiconductor is reported. While the positive peaks at 1.6 eV and 1.75 eV clearly correspond to the 0-0 and 0-1 vibronic transition bands of UV-vis spectra and thus are related to crystalline regions, the shoulder at 1.9 eV corresponds to the optical response of the non-aggregated phase within the solid films. Interestingly, the 0-0 and 0-1 bands prevail also in films processed at T_3, where the bulk optical density is instead totally dominated by the high energy transitions of the amorphous-like phase (Figure 8c). Thus, even in highly disordered films, charges preferentially select the smaller energy gaps of the residual ordered phase. Nevertheless, it may also indicate some segregation of the residual crystalline phase on the top surface of the film, as also suggested by NEXAFS analysis.

The relative intensities of polaronic bands at 1.55 eV and ~1.0 eV strongly depend on the annealing temperature and thus on the microstructure. Films annealed at T_3, which show the highest structural and conformational disorder and display the strongest thermal activation of transport, exhibit the highest charge absorption around 1.0 eV, comparable to the 1.55 eV absorption. Annealing at T_2, where the highest order and the best transport properties are found, leads to the lowest absorption around 1.0 eV, with a strong prevalence of the band at 1.55 eV. The spectra signatures of films annealed at T_1 are in between the two previous cases, consistently with mild thermal activation of transport.

The bleaching at 1.9 - 2.0 eV increases going from efficient transport (T_2) to inefficient transport (T_3). Indeed, with increasing disorder of the film, the disordered phase is necessarily more involved, leading to larger energy barriers for transport.

By combining CMS with a confocal microscope (charge modulation microscopy, CMM), using a polarized probe and fixing the energy at the bleaching main peak (1.6 eV), it is possible to map the orientation of ground state transition dipole moments within the FETs channel. The degree of orientational order *DO* can be extracted for each pixel using the methodology described in Ref.[73]. A comparison of maps obtained from films annealed at T_1 and T_2 (Figure 8 d to g) highlights a high degree of molecular alignment in both cases. A marked increase in *DO* is measured in the case of T_2 annealed films (*DO* = 0.98 at T_2 vs. *DO* = 0.89 at T_1), in agreement with the relative improvement of transport properties and with a picture of stronger interconnectivity of the ordered phase in the chain alignment direction upon annealing within the melting endotherm.

In summary, a clear correlation can be observed between CMS spectra and film transport properties, consisting in an increased charge absorption of strongly relaxed polarons at 1 eV, and non-aggregated phase (high energy) bleaching contributions going from temperature independent to strongly thermal activated transport. This unequivocally indicates that the disordered phase located in between the crystalline domains constricts charge transfer through more relaxed/localized states and thus overall limits electron transport. On the contrary, annealing at T_2 increases the dimensions of crystalline domains up to a level where electrons can travel along such crystalline pathways, and thus bypass the disordered phase.

2.8. DFT calculations for neutral and charged oligomers and aggregates

Single chain DFT calculations were performed to get insight into the predicted molecular conformations of PThDPPThF4. The torsional conformation subspace was investigated, namely the dihedral angles δ_1, δ_2, connecting the Th and DPP units, and δ_3, which connects the Th and F4 units (Figure 9a). A tetramer (n = 4) was considered representative for the polymer chain. The dihedral conformation space was further simplified for computational reasons, considering the conformations belonging to the angles δ and $2\pi - \delta$ as energetically equivalent. In Figure 9a the two most stable DFT optimized oligomer structures are reported, namely *conf*-1 and *conf*-2. They are characterized by δ_3 in a *syn*- and *anti*-conformation respectively, with δ_1 and δ_2 featuring the sulphur of the Th unit on the same side as the lactam-N of the DPP unit. To note, *conf*-1 and *conf*-2 are mostly degenerate (in vacuum) and their energy difference falls within the DFT accuracy (<

0.01 kcal/mol). We further explored the conformational space by combining δ_1, δ_2 and δ_3, the results are reported in SI (Section 2.14). The first class of conformers (referred to as *conf*-n, Figure 9a) that are the most stable and the closest in energy to *conf*-1 and *conf*-2 are characterized by the sulphur of the Th unit pointing to the carbonyl-O of the DPP unit and have an energy difference higher than 10 kcal/mol (with respect to the most stable conformers). These computational findings support structural analysis by solid state NMR. As evident by the NMR results, solid state effects cause a stabilization of *conf*-2 (i.e. δ_3 = *anti*-) rather than *conf*-1, therefore the latter was not further considered.

Starting from *conf*-2 oligomer, physical (van der Waals) dimers (i.e. aggregates) were optimized to calculate the most stable packing structure and the inter-molecular interactions at the molecular scale. Two dimers were investigated, as reported in Figure 9b, called H- and J-dimer due to their face-to-face (co-facial) or slide packing, respectively. The J-dimer is energetically more stable by 5 kcal/mol than the H-dimer. In the J-dimer, there is a slide-packing interaction (i.e. DPP unit of one chain interacting with the thiophene ring of the other chain) and the computed intermolecular distance is of 3.439 Å. In the H-dimer, there is a cofacial interaction (i.e. DPP unit of one chain interacting with the DPP of the other) and the intermolecular distance computed is 3.410 Å.

Also for the case of the dimer, the computational findings support the NMR observations, namely a polymer stacking configuration that does not involve any cofacial, H-type stacking of the PThDPPThF4 polymer chains rather than J-type stacking.

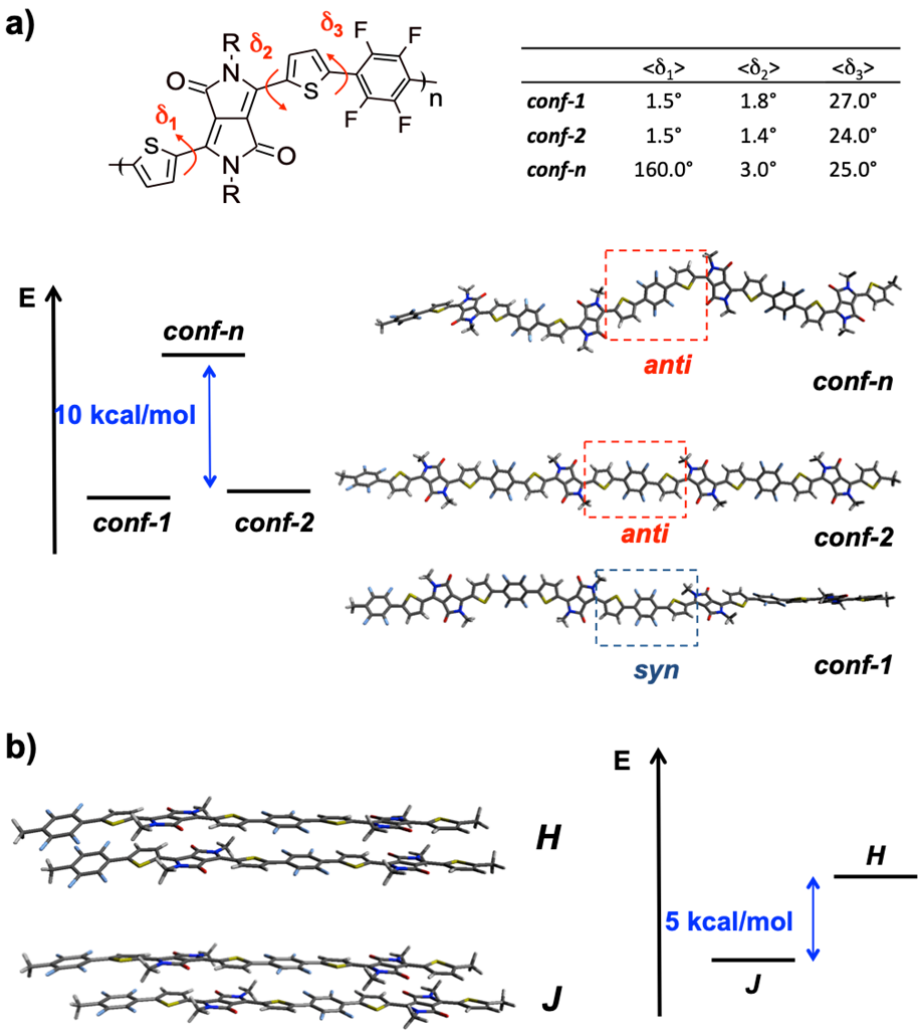

	$<\delta_1>$	$<\delta_2>$	$<\delta_3>$
conf-1	1.5°	1.8°	27.0°
conf-2	1.5°	1.4°	24.0°
conf-n	160.0°	3.0°	25.0°

Figure 9: Calculated minimum energy conformations. a) Dihedral angles investigated for the conformational analysis; most stable conformers (*conf*-1, *conf*-2 and *conf*-n) derived from DFT (ω-B97X-D/6-311G*) calculations and computed enthalpy differences. Owing to the simplification of the conformation space, for $\delta_{1,2}$, conformers characterized by the sulphur of the thiophene rings pointing toward the nitrogen heteroatom or toward the oxygen were considered. Analogously, for δ_3, we considered the so-called *syn*- and *anti*- conformations, namely the two Th units, as separated by the F4 unit, in *syn*- or *anti*-conformation with each other. b) DFT optimized H (up) and J (down) dimers end the respective enthalpy difference.

We then computed the structure and the optical properties of the most stable PThDPPThF4 charged single chain oligomer and dimer by means of DFT and TD-DFT calculations in the unrestricted scheme (UDFT and TD-UDFT). From the analysis of the structural relaxations and polaron spin density delocalization, the polaron is localized over three repeat units in the charged oligomers regardless of the conformer considered

495 (see SI Figure S37-S38).[74, 75, 76] By considering the most stable charged dimers instead, H- and J-type
496 stacking results in different spin delocalization. In the H-type dimer, the spin is mainly localized on a single
497 chain featuring a prevalent intra-molecular character, whereas in the J-type dimer the polaron spin density is
498 inter-molecularly delocalized, as reported in Figure 10. Figure 10 includes also the TD-DFT polaron optical
499 transitions for the three cases, namely the oligomer, H- and J-type dimer. Care should be taken regarding
500 band assignments because TD-DFT calculations of charged conjugated species can drastically underestimate
501 the energy of each electronic transitions (although this effect should be alleviated by using range-separated
502 functionals, as the one considered here).[77] Moreover, the band intensity can also be miscomputed, especially
503 for high energy and/or diffuse (Rydberg character) excited states.[78, 79, 80] However, the low energy transition
504 range can be confidently assigned and compared with the experimental CMS transitions. Both the oligomer
505 and the dimers show low energy polaron transitions in the 0.6 - 0.9 eV region. For the oligomer we
506 computed one intense band at 0.82 eV, mainly related to the (highest) SOMOα to the (lowest) SUMOα
507 transitions. The H-dimer features the same polaron transition, however with a reduced oscillator strength
508 than the oligomer. For the J-dimer, the transition is computed relatively red-shifted with respect the two
509 previous cases, at 0.79 eV, with a lower oscillator strength with respect to the oligomer case.
510 In summary, three observations are drawn: *i*) single chains show a more intense low energy polaron
511 transition than aggregates; *ii*) for those aggregates where the polaron spin density is localized on one chain
512 (i.e. H-type), the low energy optical transition has the same energy as in the single chain case, and *iii*) for
513 those aggregates featuring an inter-molecular delocalization of the polaron (i.e. J-type), the low energy
514 optical transition is red-shifted.
515 The computed band at 0.8 eV can be assigned to the CMS band observed in the NIR region around 1.0 eV.
516 For the case of T_3 processed films, the optical behavior is associated with the characteristics of a single chain,
517 therefore the intensity of the 1.0 eV polaron band is higher than that of the more crystalline films. For the
518 case of T_1 or T_2 annealed films, namely those with an extended degree of order and/or crystallinity, the
519 intensity of the NIR band around 1.0 eV is partially quenched by inter-molecular interactions and spin
520 delocalization, as computed for the dimeric aggregates.
521 The assignment of the CMS band at 1.55 eV is however not straightforward. TD-DFT calculations on
522 charged dimers predict a polaron transition at 1.0 - 1.1 eV and at 1.18 eV for the single oligomer. These
523 bands, most probably underestimated in energy, might be tentatively assigned to the observed band at 1.55
524 eV. For such computed transitions, the oscillator strength is higher for the dimers than for the oligomer. This
525 observation correlates with the observed behavior for the CMS band at 1.55 eV, which shows a higher
526 intensity for T_2 and T_1 with respect to T_3 annealed films.
527 Therefore, DFT calculations predict a J-dimer (i.e. the most stable computed aggregate structure) that
528 features an inter-molecular polaron spin delocalization, with the low-energy optical transition at 0.8 eV
529 showing a lower oscillator strength than the one computed for the single chain. The higher energy polaron
530 optical transition is computed at 1.0 eV, featuring a higher oscillator strength than for the oligomer. These
531 observations suggest that the CMS bands are probing polaron species, which, for the cases of T_1 and T_2

annealed films, are inter-molecularly delocalized, recalling similar observations for polycrystalline small-molecule films based on TIPS-pentacene.[81]

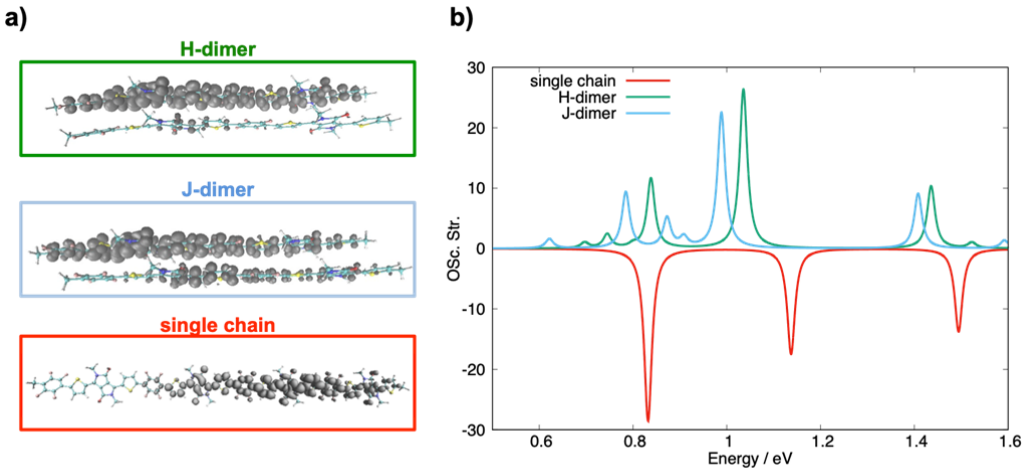

Figure 10: Spin density distribution. a) Computed UDFT (ω-UB97X-D/6-311G*) spin density for the charged (-1) species of the single chain (i.e. *conf*-2) and H- and J- dimers (both *alpha* and *beta* spin density are highlighted in grey, isosurface values 0.0003). b) Computed TD-UDFT optical polaron transitions for single chain (red), H- (green) and J-dimer (cyano).

3. Conclusions

We have shown that combined uniaxial alignment and rationally selected thermal annealing procedures of films of PThDPPThF4 strongly enhance field-effect transistor properties, culminating in a thermally independent transport regime close to room temperature. Fast scanning calorimetry probes thermal transitions in thin films and allows the selection of three characteristic annealing temperatures: T_1 below, T_2 within and T_3 above the melting temperature T_m. The results collected from FSC, optical and structural characterization can be rationalized as follows. Upon uniaxial alignment through solution processing and mild annealing (T_1), films with a relatively high crystalline content and a well-defined supramolecularly oriented organization are obtained. Annealing within the melting temperature range and near T_m (T_2), causes a fraction of thinner crystals to melt. Non-molten domains retain the orientation gained from directional processing, and grow parallel and perpendicular to the chain direction. As a result, upon T_2 annealing, oriented crystalline lamellae of increased thickness are observed. Compared to T_1 and T_2 treated films, melting at T_3 erases thermal history and chain orientation. Subsequent crystallization and solidification from the melt leads to a reduced amount of crystals and more amorphous films. These crystals are smaller and randomly oriented, and characterized by a larger average π-stacking distance owing to higher conformational disorder. A sketch of the structural modification upon the different annealing conditions is proposed in Figure 11.

Charge modulation spectroscopy measurements indicate that charged states characterized by strongly different energetic relaxation are involved in electron transport. More relaxed states, linked to higher

559 transport barriers, are associated with the non-aggregated, disordered domains, while less relaxed states,
560 linked to lower transport barriers, are associated with the more ordered, crystalline domains. The relative
561 contribution of molecularly ordered and disordered regions to transport is manipulated using different
562 thermal treatments, resulting in different degrees of energetic disorder within FETs and thus in a strong
563 modulation of the thermal barriers to electron transport. A transport improvement with lamellar thickening,
564 obtained upon annealing at T_2, is generally expected in semicrystalline polymers,[82] but it has been rarely
565 demonstrated,[83, 84] especially in solution processed films and FET architectures. Owing to the retention of
566 backbone orientation upon annealing at T_2, we were able to observe that energetic barriers for charge transfer
567 are strongly reduced exclusively in the direction of chain alignment, where effective interconnectivity of
568 ordered regions can be more easily gained, leading to temperature-independent electron transport near room
569 temperature. In contrast, in the direction perpendicular to the backbone, thermal charge transport barriers are
570 independent whether the material is annealed at T_1 or T_2, which is not surprising as in the π-stacking
571 direction coherence length is much smaller in any case. Combining thermal, structural, optical and electrical
572 characterization with computational investigation, a picture can be drawn, in which PThDPPThF4 crystalline
573 domains are energetically highly ordered and allow for superior electron coupling, up to inter-molecular
574 charge delocalization, in virtue of chains co-planarity and, as suggested by ab-initio computation, J-type
575 aggregation. Moreover, efficient transport through interconnected crystalline domains via chain extended
576 molecules, assisted by the increased co-planarity of molecules upon annealing at T_2, is needed to realize the
577 observed improvement in FET charge transport, characterized by high and temperature independent electron
578 mobility. Insufficient interconnection of crystalline domains limits instead transport in films annealed at T_1,
579 and even more drastically in films processed at T_3, dominated by disorder.
580 In conclusion, for a low-molecular weight, high performance electron transporting copolymer, synthesized
581 free of homocoupling defects by a simple direct arylation polycondensation protocol, we have identified key
582 parameters required to induce a transition from thermally activated to temperature independent and charge
583 density independent, single crystal like electron transport. The microstructure needed for such transport
584 behavior is characterized by *i*) a crystalline phase with planar molecular conformation, which is the low-
585 energy phase selectively populated by charges, along with *ii*) a molecular J-like packing, allowing for charge
586 delocalization across different chains within such phase and iii) an efficient inter-crystallite transport,
587 allowing to bypass the high-energy disordered phases present in the film. These results rationalize the link
588 between complex, semicrystalline polymer thin film microstructure and more efficient charge transport
589 beyond thermally activated regimes. As such, they can pave the way for a new generation of higher
590 performance polymer electronics, suitable for a wider range of applications, such as ultra-high resolution
591 displays and wireless communications, currently not accessible because of limited carrier mobilities.

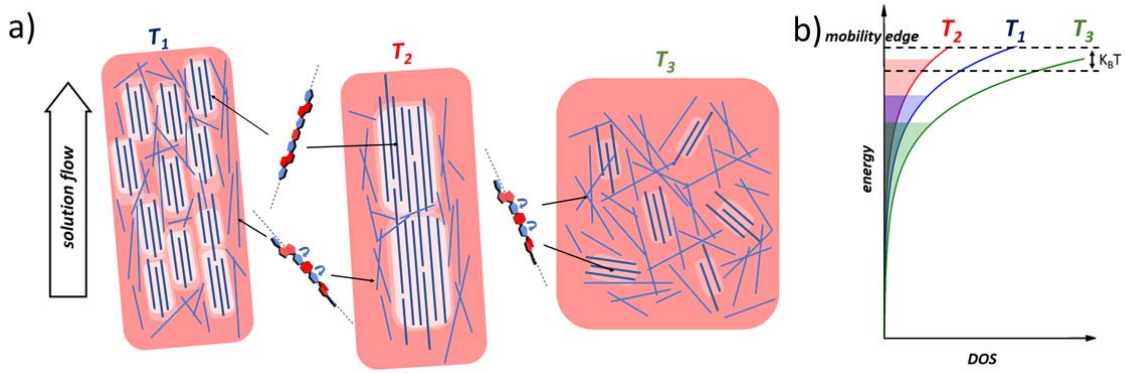

Figure 11: Structure-transport property relationship. a) Proposed sketch for the changes in the functional morphology, i.e. the morphology of the molecules involved in charge transport, of PThDPPThF4 films upon annealing at T_1, T_2 and T_3; thicker lines represent crystalline polymer segments; brighter areas evidence superior electron coupling. b) Proposed energetic diagram describing transport within films annealed at T_1, T_2 and T_3. According to a mobility edge model, the energy barrier for charge transport is defined as the difference between the mobility edge and the energy of localized states. The DOS tail variation induced by the applied thermal annealing allows for a modulation of transport barriers: thermal annealing at T_2 leads to energy barriers inferior to k_BT, i.e., around room temperature thermal fluctuations enable charge releasing from shallow traps to extended mobile states.

Acknowledgments

M. C. thanks D. Natali for insightful discussions. M. S. and F. N. thank M. Hagios and A. Warmbold for SEC and bulk DSC measurements, respectively. This work was financially supported by the European Research Council (ERC) under the European Union's Horizon 2020 research and innovation programme "HEROIC", grant agreement 638059. M. S. acknowledges funding from the DFG (SO 1213/8-1). N. S. acknowledges the financial support of the US National Science Foundation through the DMREF program (DMR-1729737). D. F. acknowledges the Deutsche Forschungsgemeinschaft (DFG) for a Principal Investigator grant (FA 1502/1-1). Part of this work was carried out on the SAXS/WAXS and Soft X-ray Beamlines at the Australian Synchrotron, part of ANSTO and at Polifab, the micro- and nano-technology center of the Politecnico di Milano.

References

1. Caironi, M., Noh, Y. Y. (eds). *Large Area and Flexible Electronics*. Wiley-VCH Verlag GmbH & Co. KGaA, 2015.

2. Guo, X., et al. Current Status and Opportunities of Organic Thin-Film Transistor Technologies. *IEEE Trans. Electron Dev.* **64**, 1906-1921 (2017).

3. Sirringhaus, H. Materials and Applications for Solution-Processed Organic Field-Effect Transistors. *P. IEEE* **97**, 1570-1579 (2009).

4. Chang, J. S., Facchetti, A. F., Reuss, R. A Circuits and Systems Perspective of Organic/Printed Electronics: Review, Challenges, and Contemporary and Emerging Design Approaches. *IEEE J. Em. Sel. Top. C.* **7**, 7-26 (2017).

5. Kaltenbrunner, M., et al. An ultra-lightweight design for imperceptible plastic electronics. *Nature* **499**, 458-463 (2013).

6. Troisi, A. The speed limit for sequential charge hopping in molecular materials. *Org. Electron.* **12**, 1988-1991 (2011).

7. Sirringhaus, H. 25th Anniversary Article: Organic Field-Effect Transistors: The Path Beyond Amorphous Silicon. *Adv. Mater.* **26**, 1319-1335 (2014).

8. Berggren, M., et al. Browsing the Real World using Organic Electronics, Si□Chips, and a Human Touch. *Adv. Mater.* **28**, 1911-1916 (2016).

9. Baeg, K.-J., Caironi, M., Noh, Y.-Y. Toward Printed Integrated Circuits based on Unipolar or Ambipolar Polymer Semiconductors. *Adv. Mater.* **25**, 4210-4244 (2013).

10. Wong, W. S., Salleo, A. *Flexible electronics: materials and applications*, vol. 11. Springer Science & Business Media, 2009.

11. Liu, Y., Pharr, M., Salvatore, G. A. Lab-on-Skin: A Review of Flexible and Stretchable Electronics for Wearable Health Monitoring. *ACS Nano* **11**, 9614-9635 (2017).

12. Shi, L., et al. Design and effective synthesis methods for high-performance polymer semiconductors in organic field-effect transistors. *Mater. Chem. Front.* **1**, 2423-2456 (2017).

13. Paterson, A. F., et al. Recent Progress in High-Mobility Organic Transistors: A Reality Check. *Adv. Mater.* **30**, 1801079 (2018).

14. Bucella, S. G., et al. Macroscopic and high-throughput printing of aligned nanostructured polymer semiconductors for MHz large-area electronics. *Nat. Commun.* **6**, 8394 (2015).

15. Zhou, X., et al. Balanced ambipolar organic thin-film transistors operated under ambient conditions: Role of the donor moiety in BDOPV-based conjugated copolymers. *Chem. Mater.* **27**, 1815-1820 (2015).

16. Dai, Y.-Z., et al. Embedding electron-deficient nitrogen atoms in polymer backbone towards high performance n-type polymer field-effect transistors. *Chem. Sci.* **7**, 5753-5757 (2016).

17. Chen, Z., et al. High□Performance Ambipolar Diketopyrrolopyrrole□Thieno [3, 2□b] thiophene Copolymer Field□Effect Transistors with Balanced Hole and Electron Mobilities. *Adv. Mater.* **24**, 647-652 (2012).

18. Gao, Y., et al. High Mobility Ambipolar Diketopyrrolopyrrole□Based Conjugated Polymer Synthesized Via Direct Arylation Polycondensation. *Adv. Mater.***27**, 6753-6759 (2015).

19. Gao, Y., et al. Multifluorination toward High□Mobility Ambipolar and Unipolar n□Type Donor–Acceptor Conjugated Polymers Based on Isoindigo. *Adv. Mater.* **29**, 1606217 (2017).

20. Lee, J., et al. Solution-processable ambipolar diketopyrrolopyrrole–selenophene polymer with unprecedentedly high hole and electron mobilities. *J. Am. Chem. Soc.* **134**, 20713-20721 (2012).

21. Lee, J., et al. Boosting the Ambipolar Performance of Solution-Processable Polymer Semiconductors via Hybrid Side-Chain Engineering. *J. Am. Chem. Soc.* **135**, 9540-9547 (2013).

22. Kang, B., et al. Side-chain-induced rigid backbone organization of polymer semiconductors through semifluoroalkyl side chains. *J. Am. Chem. Soc.* **138**, 3679-3686 (2016).

23. Sun, B., et al. Record high electron mobility of 6.3 cm2V− 1s− 1 achieved for polymer semiconductors using a new building block. *Adv. Mater.* **26**, 2636-2642 (2014).

24. Zhao, Z., et al. High□Performance, Air□Stable Field□Effect Transistors Based on Heteroatom□Substituted Naphthalenediimide□Benzothiadiazole Copolymers Exhibiting Ultrahigh Electron Mobility up to 8.5 cm V^{-1} s^{-1}. *Adv. Mater.* **29**, 1602410 (2017).

25. Sung, M. J., et al. High□Mobility Naphthalene Diimide and Selenophene□Vinylene□Selenophene□Based Conjugated Polymer: n□Channel Organic Field□Effect Transistors and Structure–Property Relationship. *Adv. Funct. Mater.* **26**, 4984-4997 (2016).

26. Fallon, K. J., et al. Indolo-naphthyridine-6, 13-dione Thiophene Building Block for Conjugated Polymer Electronics: Molecular Origin of Ultrahigh n-Type Mobility. *Chem. Mater.* **28**, 8366-8378 (2016).

27. Zhenjie, N., et al. Quinoline-Flanked Diketopyrrolopyrrole Copolymers Breaking through Electron Mobility over 6 cm2 V^{-1} s^{-1} in Flexible Thin Film Devices. *Adv. Mater.* **30**, 1704843 (2018).

28. Minder, N. A., et al. Band□Like Electron Transport in Organic Transistors and Implication of the Molecular Structure for Performance Optimization. *Adv. Mater.* **24**, 503-508 (2012).

29. Kim, B. J., et al. Electrical transport through single nanowires of dialkyl perylene diimide. *J. Phys. Chem. C* **117**, 10743-10749 (2013).

30. Minder, N. A., et al. Tailoring the molecular structure to suppress extrinsic disorder in organic transistors. *Adv. Mater.* **26**, 1254-1260 (2014).

31. Krupskaya, Y., et al. Band□Like Electron Transport with Record□High Mobility in the TCNQ Family. *Adv. Mater.* **27**, 2453-2458 (2015).

32. Xu, X., et al. Electron Mobility Exceeding 10 cm^2 V^{-1} s^{-1} and Band□Like Charge Transport in Solution□Processed n□Channel Organic Thin□Film Transistors. *Adv. Mater.* **28**, 5276-5283 (2016).

33. Mei, Y., et al. Crossover from band-like to thermally activated charge transport in organic transistors due to strain-induced traps. *P. Natl. Acad. Sci. USA*, 201705164 (2017).

34. Lee, J., et al. Thin films of highly planar semiconductor polymers exhibiting band-like transport at room temperature. *J. Am. Chem. Soc.* **137**, 7990-7993 (2015).

35. Schott, S., et al. Charge□Transport Anisotropy in a Uniaxially Aligned Diketopyrrolopyrrole□Based Copolymer. *Adv. Mater.* **27**, 7356-7364 (2015).

36. Yamashita, Y., et al. Transition Between Band and Hopping Transport in Polymer Field□Effect Transistors. *Adv. Mater.* **26**, 8169-8173 (2014).

37. Yamashita, Y., et al. Mobility Exceeding 10 cm2/(V· s) in Donor–Acceptor Polymer Transistors with Band-like Charge Transport. *Chem. Mater.* **28**, 420-424 (2016).

38. Senanayak, S. P., et al. Room-temperature bandlike transport and Hall effect in a high-mobility ambipolar polymer. *Phys. Rev. B* **91**, 115302 (2015).

39. Park, J. H., et al. A Fluorinated Phenylene Unit as a Building Block for High□Performance n□Type Semiconducting Polymer. *Adv. Mater.* **25**, 2583-2588 (2013).

40. Broll, S., et al. Defect Analysis of High Electron Mobility Diketopyrrolopyrrole Copolymers Made by Direct Arylation Polycondensation. *Macromolecules* **48**, 7481-7488 (2015).

41. Martín, J., et al. On the Effect of Confinement on the Structure and Properties of Small-Molecular Organic Semiconductors. *Adv. Electron. Mater.* **4**, 1700308 (2018).

42. Martín, J., Stingelin, N., Cangialosi, D. Direct Calorimetric Observation of the Rigid Amorphous Fraction in a Semiconducting Polymer. *J. Phys. Chem. Lett.* **9**, 990-995 (2018).

43. Schawe, J. E. K. Influence of processing conditions on polymer crystallization measured by fast scanning DSC. *J. Therm. Anal. Calorim.* **116**, 1165-1173 (2014).

44. Shin, Y.-h., et al. Regioregular Polymer Analogous Thionation of Naphthalene Diimide–Bithiophene Copolymers. *Macromolecules* **51**, 984-991 (2018).

45. Gibbs, J. W. *Collected Works*. Yale Univ. Press, 1948.

46. Strobl, G. *The Physics of Polymers: conceps for understanding their structures and behaviour*. Springer, 2007.

47. Martin, J., et al. Temperature-Dependence of Persistence Length Affects Phenomenological Descriptions of Aligning Interactions in Nematic Semiconducting Polymers. *Chem. Mater.* **30**, 748-761 (2018).

48. Khim, D., et al. Uniaxial Alignment of Conjugated Polymer Films for High-Performance Organic Field-Effect Transistors. *Adv. Mater.* **30**, 1705463 (2018).

49. Luzio, A., et al. Control of charge transport in a semiconducting copolymer by solvent-induced long-range order. *Sci. Rep.* **3**, 3425 (2013).

50. Nahid, M. M., et al. NEXAFS spectroscopy of conjugated polymers. *Eur. Polym. J.* **81**, 532-554 (2016).

51. Gross, Y. M., et al. Tuning Aggregation by Regioregularity for High-Performance n-Type P(NDI2OD-T2) Donor–Acceptor Copolymers. *Macromolecules* **50**, 5353-5366 (2017).

52. Trefz, D., et al. Tuning Orientational Order of Highly Aggregating P(NDI2OD-T2) by Solvent Vapor Annealing and Blade Coating. *Macromolecules* **52**, 43–54 (2018).

53. Rouger, L., et al. Ultrafast acquisition of 1 H-1 H dipolar correlation experiments in spinning elastomers. *J. Magn. Reson.* **277**, 30-35 (2017).

54. Do, K., et al. Impact of Fluorine Substituents on π□Conjugated Polymer Main□Chain Conformations, Packing, and Electronic Couplings. *Adv. Mater.* **28**, 8197-8205 (2016).

55. Hansen, M. R., Graf, R., Spiess, H. W. Interplay of structure and dynamics in functional macromolecular and supramolecular systems as revealed by magnetic resonance spectroscopy. *Chem. Rev.* **116**, 1272-1308 (2015).

56. Liu, C., et al. Device Physics of Contact Issues for the Overestimation and Underestimation of Carrier Mobility in Field-Effect Transistors. *Phys. Rev. Appl.* **8**, 034020 (2017).

57. Förster, A., et al. Influence of Electric Fields on the Electron Transport in Donor–Acceptor Polymers. *The Journal of Physical Chemistry C* **121**, 3714-3723 (2017).

58. Nikiforov, G. O., et al. Current□Induced Joule Heating and Electrical Field Effects in Low Temperature Measurements on TIPS Pentacene Thin Film Transistors. *Adv. Electron. Mater.* **2**, 1600163 (2016).

59. Sze, S. M., Ng, K. K. *Physics of Semiconductor Devices, 3rd Edition*, 3rd Edition edn. John Wiley & Sons, Inc., 2006.

60. Toman, P., et al. Modelling of the charge carrier mobility in disordered linear polymer materials. *Phys. Chem. Chem. Phys.* **19**, 7760-7771 (2017).

61. Klauk, H. *Organic electronics II: more materials and applications*, vol. 2. John Wiley & Sons, 2012.

62. Choi, H. H., et al. Critical assessment of charge mobility extraction in FETs. *Nat. Mater.* **17**, 2-7 (2017).

63. Yamashita, Y., et al. Mobility Exceeding 10 cm2/(V·s) in Donor–Acceptor Polymer Transistors with Band-like Charge Transport. *Chem. Mater.* **28**, 420-424 (2016).

64. Tseng, H. R., et al. High mobility field effect transistors based on macroscopically oriented regioregular copolymers. *Nano Lett.* **12**, 6353-6357 (2012).

65. Gao, Y., et al. High Mobility Ambipolar Diketopyrrolopyrrole-Based Conjugated Polymer Synthesized Via Direct Arylation Polycondensation. *Adv. Mater.* **27**, 6753-6759 (2015).

66. Caironi, M., et al. Very Low Degree of Energetic Disorder as the Origin of High Mobility in an n-channel Polymer Semiconductor. *Adv. Funct. Mater.* **21**, 3371-3381 (2011).

67. Luzio, A., et al. Hybrid Nanodielectrics for Low□Voltage Organic Electronics. *Adv. Funct. Mater.* **24**, 1790-1798 (2014).

68. Li, J., Sun, Z., Yan, F. Solution Processable Low□Voltage Organic Thin Film Transistors with High□k Relaxor Ferroelectric Polymer as Gate Insulator. *Adv. Mater.* **24**, 88-93 (2012).

69. Pal, B. N., et al. Solution-deposited sodium beta-alumina gate dielectrics for low-voltage and transparent field-effect transistors. *Nat. Mater.* **8**, 898-903 (2009).

70. Ortiz, R. P., Facchetti, A., Marks, T. J. High-k organic, inorganic, and hybrid dielectrics for low-voltage organic field-effect transistors. *Chem. Rev.* **110**, 205-239 (2009).

71. Kim, M.-G., et al. Low-temperature fabrication of high-performance metal oxide thin-film electronics via combustion processing. *Nat. Mater.* **10**, 382-388 (2011).

72. Sekitani, T., et al. Organic Nonvolatile Memory Transistors for Flexible Sensor Arrays. *Science* **326**, 1516-1519 (2009).

73. Martino, N., et al. Mapping Orientational Order of Charge-Probed Domains in a Semiconducting Polymer. *ACS Nano* **8**, 5968-5978 (2014).

74. Francis, C., et al. Raman spectroscopy and microscopy of electrochemically and chemically doped high-mobility semiconducting polymers. *J. Mater. Chem. C* **5**, 6176-6184 (2017).

75. Kahmann, S., et al. Polarons in Narrow Band Gap Polymers Probed over the Entire Infrared Range: A Joint Experimental and Theoretical Investigation. *J. Phys. Chem. Lett.* **7**, 4438-4444 (2016).

76. Steyrleuthner, R., et al. Impact of morphology on polaron delocalization in a semicrystalline conjugated polymer. *Phys. Chem. Chem. Phys.* **19**, 3627-3639 (2017).

77. Fazzi, D., Caironi, M., Castiglioni, C. Quantum chemical insights in the prediction of charge transport parameters for a naphthalenetetracarboxidiimide based copolymer with enhanced electron mobility. *J. Am. Chem. Soc.* **133**, 47 (2011).

78. Zheng, Z., et al. Effect of Solid-State Polarization on Charge-Transfer Excitations and Transport Levels at Organic Interfaces from a Screened Range-Separated Hybrid Functional. *J. Phys. Chem. Lett.* **8**, 3277-3283 (2017).

79. Dreuw, A., Head-Gordon, M. Failure of Time-Dependent Density Functional Theory for Long-Range Charge-Transfer Excited States: The Zincbacteriochlorin−Bacteriochlorin and Bacteriochlorophyll−Spheroidene Complexes. *J. Am. Chem. Soc.* **126**, 4007-4016 (2004).

80. Baer, R., Livshits, E., Salzner, U. Tuned Range-Separated Hybrids in Density Functional Theory. *Annu. Rev. Phys. Chem.* **61**, 85-109 (2010).

81. Eggeman, A. S., et al. Measurement of molecular motion in organic semiconductors by thermal diffuse electron scattering. *Nat. Mater.* **12**, 1045-1049 (2013).

82. Koch, F. P. V., et al. The impact of molecular weight on microstructure and charge transport in semicrystalline polymer semiconductors–poly (3-hexylthiophene), a model study. *Prog. Polym. Sci.* **38**, 1978-1989 (2013).

83. Müller, C., et al. Enhanced charge-carrier mobility in high-pressure-crystallized poly (3-hexylthiophene). *Macromolecules* **44**, 1221-1225 (2011).

84. Baklar, M. A., et al. Solid State Processing of Organic Semiconductors. *Adv. Mater.* **22**, 3942-3947 (2010).